

Achieving Efficient Alkaline Hydrogen Evolution Reaction over a Ni₅P₄ Catalyst Incorporating Single-Atomic Ru Sites

Qun He, Dong Tian, Hongliang Jiang, Dengfeng Cao, Shiqiang Wei, Daobin Liu, Pin Song, Yue Lin, and Li Song*

Developing efficient electrocatalysts for alkaline water electrolysis is central to substantial progress of alkaline hydrogen production. Herein, a Ni₅P₄ electrocatalyst incorporating single-atom Ru (Ni₅P₄-Ru) is synthesized through the filling of Ru³⁺ species into the metal vacancies of nickel hydroxides and subsequent phosphorization treatment. Electron paramagnetic resonance spectroscopy, X-ray-based measurements, and electron microscopy observations confirm the strong interaction between the nickel-vacancy defect and Ru cation, resulting in more than 3.83 wt% single-atom Ru incorporation in the obtained Ni₅P₄-Ru. The Ni₅P₄-Ru as an alkaline hydrogen evolution reaction catalyst achieves low onset potential of 17 mV and an overpotential of 54 mV at a current density of 10 mA cm⁻² together with a small Tafel slope of 52.0 mV decade⁻¹ and long-term stability. Further spectroscopy analyses combined with density functional theory calculations reveal that the doped Ru sites can cause localized structure polarization, which brings the low energy barrier for water dissociation on Ru site and the optimized hydrogen adsorption free energy on the interstitial site, well rationalizing the experimental reactivity.

development of Pt-free electrocatalysts for alkaline HER is still challenging due to their sluggish reaction kinetics of water activation, but appealing.^[7–9] In alkaline condition, water molecule undergoes an Volmer step (H₂O + e⁻ + * → H_{ads} + OH⁻) to achieve water dissociation and the formation of adsorbed hydrogen. The adsorbed hydrogen would occur desorption process to release hydrogen molecule (Heyrovsky step: H_{ads} + H₂O + e⁻ → H₂ + OH⁻ + *). Nevertheless, the high energy barrier for water dissociation and the unsatisfactory hydrogen desorption hamper the overall HER activity.^[10] In this regard, the electronic regulation of catalysts is considered as a strategy to improve HER performance.^[11–15] For instance, the N incorporation in metallic CoS₂ led to the optimal free energy of hydrogen adsorption, resulting in improved HER energetics.^[14] The Mn doping brought metallic

Hydrogen production from electrochemical water splitting is regarded as a promising approach to mitigate the dependence on fossil fuels.^[1,2] To date, many non-Pt catalysts with Pt-comparable hydrogen evolution reaction (HER) activity in acidic medium have been reported.^[3–6] However, the

CoS₂ with the optimized reaction process for hydrogen adsorption, as indicated with the zero-close Gibbs free energy.^[15] In addition, developing HER catalysts through the positive incorporation of active HER sites into supports is also a feasible method, but rarely reported.^[16–18] Recently, the incorporation of high-density single-atom sites into supports to achieve the highest atomic efficiency (mainly noble metal atoms) and the empowered catalytic property is in frontier.^[19,20] Unfortunately, achieving high density and single-atom incorporation is always challenging especially for non-carbon materials, such as hydroxides, oxides, nitrides, sulfides, and phosphides.^[21–24] Taking these views into account, it is believed that the proper integration design of electronic regulation and single-atom incorporation would achieve superior HER catalysis in alkaline. In this work, as a model example, the relatively low-cost Ru was chosen as the incorporated element due to its similar metal-hydrogen bond strength compared to that of Pt and apparent HER activity.^[17,25] The nickel-vacancy-rich nickel hydroxides as support precursor stabilized the Ru species. Meticulous characterizations, including electron paramagnetic resonance (EPR) and X-ray absorption fine structure spectroscopy (XAFS), verified the successful coupling of the Ru site with oxygen near the nickel vacancy. The final Ni₅P₄-Ru nanoparticles were obtained through subsequent phosphorization treatment. Combining with the analysis from high-angle annular dark-field scanning transmission electron microscopy (HAADF-STEM) and X-ray absorption near-edge structure spectra (XANES), single-atom

Q. He, Prof. H. Jiang, D. Cao, S. Wei, Dr. Y. Lin, Prof. L. Song
National Synchrotron Radiation Laboratory
Hefei National Laboratory for Physical Sciences at the Microscale
CAS Center for Excellence in Nanoscience
University of Science and Technology of China
Hefei, Anhui 230029, China
E-mail: song2012@ustc.edu.cn

D. Tian
State Key Laboratory of Complex Nonferrous Metal
Resources Clean Utilization
Kunming University of Science and Technology
Kunming 650093, China

Prof. H. Jiang
School of Chemical Engineering
East China University of Science and Technology
Shanghai 200237, China

Dr. D. Liu, Dr. P. Song
School of Materials Science and Engineering
Nanyang Technological University
Singapore 639798, Singapore

 The ORCID identification number(s) for the author(s) of this article can be found under <https://doi.org/10.1002/adma.201906972>.

DOI: 10.1002/adma.201906972

Ru sites in Ni_5P_4 and localized structure polarization were confirmed. The electrochemical measurements suggested that the obtained $\text{Ni}_5\text{P}_4\text{-Ru}$ achieved a promising HER activity with low onset potential of 17 mV and overpotential of 54 mV at current density of 10 mA cm^{-2} , together with small Tafel slope of $52.0 \text{ mV decade}^{-1}$ and long-term durability. Density functional theory (DFT) calculations explored the structural change after Ru incorporation and gave an understanding as to why the HER performance improved. Theoretical results stated that the deliberately introduced single-atom Ru sites would induce localized structure polarization, subsequently the electron-rich Ru sites benefit the HER process with low H_2O dissociation energy and the localized interstitial structure would achieve an optimized free energy for hydrogen adsorption.

The $\text{Ni}(\text{OH})_2$ with rich nickel vacancies was prepared by a propylene oxide-mediated alkalization precipitation method reported previously (namely, $\text{V-Ni}(\text{OH})_2$, see the Experimental

Section for details).^[26] The Ru^{3+} cations were stabilized with the nickel vacancies in $\text{V-Ni}(\text{OH})_2$ (recorded as $\text{V-Ni}(\text{OH})_2\text{-Ru}$) via simple impregnation method (Figure 1a, see the Experimental Section for details). Optical and electron microscopy observations as well as elemental mapping proved the obtaining of $\text{Ni}(\text{OH})_2$ and the existence of Ru in $\text{Ni}(\text{OH})_2$ (Figures S1 and S2, Supporting Information). Inductively coupled plasma-atomic emission spectra (ICP-AES) demonstrated a high mass ratio of 4.04 wt% has achieved for $\text{V-Ni}(\text{OH})_2\text{-Ru}$ (Table S1, Supporting Information). The abundant nickel vacancies in $\text{V-Ni}(\text{OH})_2$ have been proved to be vital in achieving single-atom Ru incorporation with high-density. As a reference, $\text{Ni}(\text{OH})_2$ with fewer nickel vacancies was prepared and treated with Ru cations as $\text{V-Ni}(\text{OH})_2\text{-Ru}$ (namely, $\text{P-Ni}(\text{OH})_2$ and $\text{P-Ni}(\text{OH})_2\text{-Ru}$, respectively, see the Experimental Section).^[26] A very low Ru/Ni ratio (0.08 wt%) has obtained for $\text{P-Ni}(\text{OH})_2\text{-Ru}$ (Table S1, Supporting Information). EPR results further evidenced this conclusion

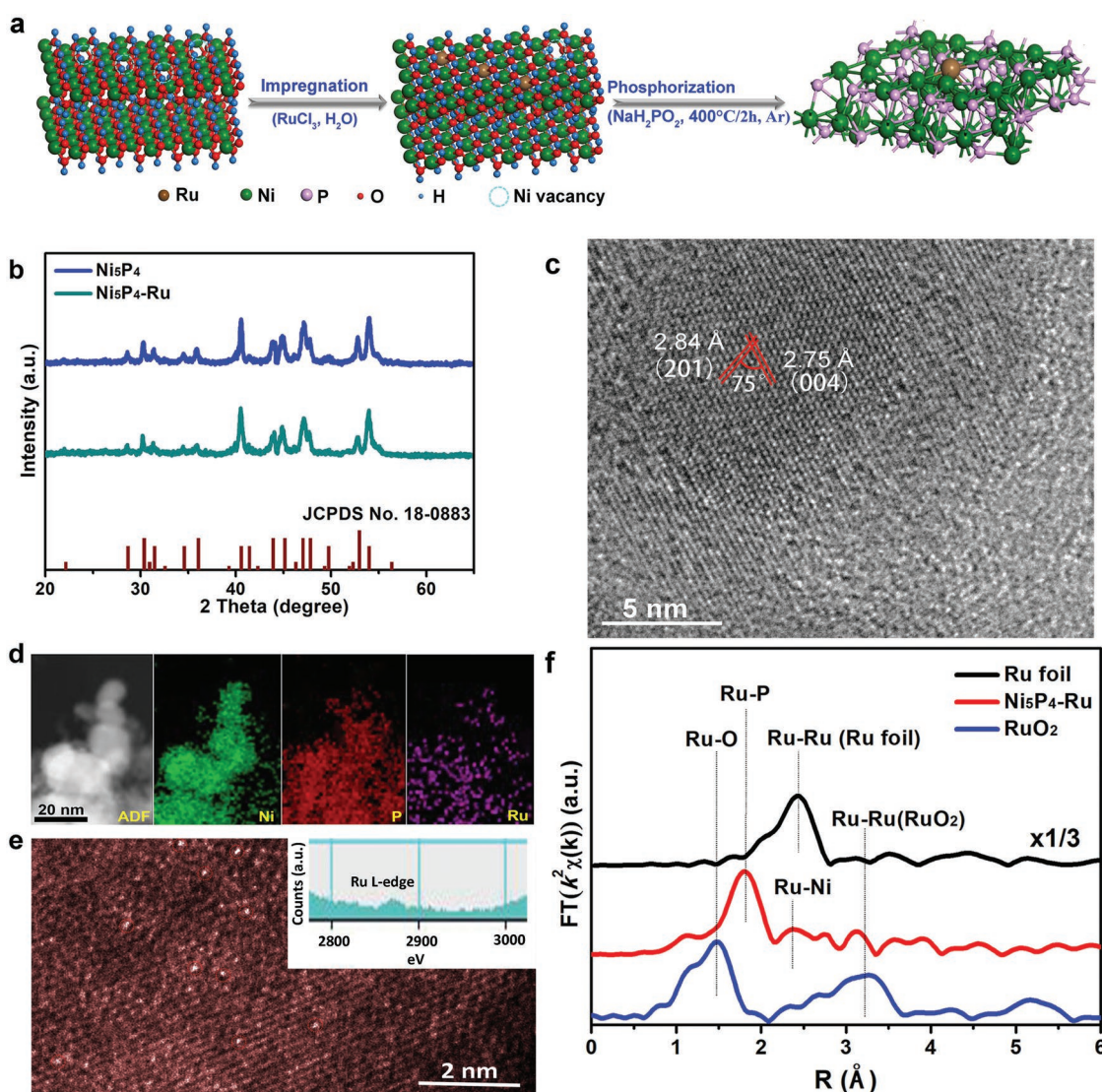


Figure 1. a) Schematic diagram for the synthesis of $\text{Ni}_5\text{P}_4\text{-Ru}$. b) Typical XRD patterns of $\text{Ni}_5\text{P}_4\text{-Ru}$ and Ni_5P_4 . c) HRTEM image of $\text{Ni}_5\text{P}_4\text{-Ru}$. d) Elemental mappings of $\text{Ni}_5\text{P}_4\text{-Ru}$. e) HAADF-STEM image of $\text{Ni}_5\text{P}_4\text{-Ru}$ (inset: corresponding EELS spectrum at Ru L-edge). f) The Ru K-edge k^2 -weighted EXAFS profiles of $\text{Ni}_5\text{P}_4\text{-Ru}$, Ru foil, and RuO_2 .

(Figure S3, Supporting Information). A strong Ru³⁺ EPR signal was detected for V-Ni(OH)₂-Ru; however, no obvious Ru³⁺ signal could be seen for P-Ni(OH)₂-Ru (Figure S3a, Supporting Information).^[27] As expected, the stabilization of Ru cations by nickel vacancies has occurred, which could be attributed to the electronic coupling mechanism.^[28] It is well established that the coupling would induce the local structural perturbation in the interfaces. Now, we pay main attention to the structural exploration of V-Ni(OH)₂-Ru. EPR results showed that the Ni³⁺ signal in V-Ni(OH)₂-Ru was stronger than that in V-Ni(OH)₂, which demonstrated the existence of more Ni³⁺ (Figure S3a, Supporting Information). This was probably from the considerable electronic coupling in the interfaces.^[26] By contrast, P-Ni(OH)₂-Ru showed almost unchanged EPR signal relative to P-Ni(OH)₂ (Figure S3b, Supporting Information). These results suggested that the distinct electronic coupling should have been occurred on account of nickel vacancies, which could provide promising sites for Ru stabilization in our experiment. X-ray diffraction (XRD) patterns showed that all the diffraction peaks of V-Ni(OH)₂-Ru and V-Ni(OH)₂ coincided well with that of reported nickel-vacancy-rich Ni(OH)₂ (Figure S4, Supporting Information), suggesting the unchanged main structure after Ru incorporation.^[26] X-ray photoelectron spectra (XPS) verified the surface difference after Ru incorporation (Figures S5–S7, Supporting Information). The Ni 2p peak showed a positive shift of binding energy by 0.4 eV, which suggested the increased valence state of Ni in V-Ni(OH)₂-Ru and coincided well with the above EPR results. The Ru signal was also detected. To detect the structural information of samples, XAFS analysis was also carried out. The Ni K-edge XANES profiles exhibited that V-Ni(OH)₂-Ru had a positive absorption edge shift and reduced white line peak relative to V-Ni(OH)₂, further revealing the increased valence state of Ni in V-Ni(OH)₂-Ru (Figure S8a, Supporting Information). Their oscillation curves at the *k* range of 2–14 Å⁻¹ and the extended XAFS (EXAFS) profiles showed negligible changes, further demonstrating the consistency of main structure (Figure S8b,c, Supporting Information). It is interesting that the Ru K-edge EXAFS profile of V-Ni(OH)₂-Ru exhibited significantly reduced Ru–Cl bond relative to that of pure RuCl₃ and a peak close to Ru–O bond in RuO₂ was observed without obvious Ru–Ru bond.^[29,30] These consequences suggested that the Ru cations were stabilized by selectively bonding at nickel vacancies and therefore highly dispersed Ru sites were reasonably achieved (Figure S9, Supporting Information). In brief, highly dispersed Ru sites incorporated into V-Ni(OH)₂ have been successfully achieved via the assistance of rich nickel vacancies, which bring a strong electronic coupling to specially stabilize Ru sites.

The final phosphide nanoparticles were obtained through the subsequent phosphorization treatment (Figure S10, Supporting Information). ICP-AES analysis showed that the Ni₅P₄-Ru nanoparticles contained a high ratio of Ru (3.83 wt%), higher than most reported materials (Table S2, Supporting Information). This result revealed the feasibility of our two-step impregnation–phosphorization method in developing a high-density Ru-incorporating catalyst from V-Ni(OH)₂. XRD patterns demonstrated that the V-Ni(OH)₂ was transferred into Ni₅P₄ and the Ru-related species showed no peaks, suggesting that the Ru species were highly dispersed or sufficiently small

(JCPDS No. 18-0883; Figure 1b). High-resolution transmission electron microscopy (HRTEM) showed two continuous and ordered lattice fringes with the lattice spacings of ≈2.84 and ≈2.75 Å together with the crystal plane angle of 75°, which corresponded to the (201) and (004) planes of Ni₅P₄ (Figure 1c; Figure S11, Supporting Information). XPS results showed the coexistence of Ni, P, and Ru in Ni₅P₄-Ru and the elemental mappings revealed their uniform distribution (Figure S12, Supporting Information; Figure 1d). To prove the existing state of Ru in Ni₅P₄-Ru, HAADF-STEM measurement was performed. In Figure 1e, there are some atomically dispersed bright dots (highlighted with red circles), which represent the single Ru atoms due to its higher *Z* value than Ni and P. As considered, only metal atoms are unstable on the supports due to the high surface energy; therefore, the bonding environment of Ru needs to be verified.^[19] Here, the Ru K-edge XAFS measurements of Ni₅P₄-Ru and control samples were performed. Undoubtedly, the EXAFS profile exhibited the presence of Ru–P and Ru–Ni bonds without Ru–Ru bond, demonstrating the single-atomic Ru sites were achieved in Ni₅P₄ (Figure S13, Supporting Information; Figure 1f). The fitted Ni and Ru K-edge EXAFS results showed the detailed bond information for Ni and Ru centers and no Ru–Ru bond, further confirming the above conclusion (Figures S14 and S15 and Tables S3 and S4, Supporting Information).

The alkaline HER performance of our samples was evaluated in 1.0 M potassium hydroxide (KOH) solution. Figure 2a shows the HER linear scan voltammograms (LSV) curves of different catalysts. The Ni₅P₄-Ru achieved a current density of 10 mA cm⁻² at an overpotential of 123 mV, lower than Ni₅P₄ (289 mV). This result demonstrated the promotion role of single-atomic Ru incorporation in HER activity. The good catalytic activity of Ni₅P₄-Ru was also demonstrated by the smallest Tafel slope of 56.7 mV decade⁻¹ among these Ni-based HER catalysts, which was even comparable to that of commercial Pt/C (44.2 mV decade⁻¹; Figure 2b). To give solid performance comparison among these samples, some typical parameters including onset potential, overpotential and exchange current density were summarized in Figure 2c. Obviously, the Ni₅P₄-Ru showed an onset potential of 35 mV (evaluated from the potential achieving 1.0 mA cm⁻²), which was smaller than Ni₅P₄ (161 mV), V-Ni(OH)₂-Ru (352 mV), and V-Ni(OH)₂ (443 mV). Meanwhile, the exchange current density of Ni₅P₄-Ru (350.9 μA cm⁻²), was approximately 6.0, 26.8, 55.7 times higher than that of Ni₅P₄ (58.8 μA cm⁻²), V-Ni(OH)₂-Ru (13.1 μA cm⁻²), and V-Ni(OH)₂ (6.3 μA cm⁻²), respectively (Figure S16, Supporting Information). The high exchange current density suggested the optimal electrode kinetics of Ni₅P₄-Ru, which was also demonstrated from the largely reduced charge transfer resistance (*R*_{ct}) of Ni₅P₄-Ru measured from the electrochemical impedance spectroscopy (EIS) (Figure S17, Supporting Information). The electrochemical activities were further normalized by the electrochemical surface area (ECSA). Apparently, the Ni₅P₄-Ru showed an overpotential of 102 mV at the true value of 0.25, which was largely lower than that of Ni₅P₄ (234 mV), V-Ni(OH)₂-Ru (460 mV), and V-Ni(OH)₂ (508 mV) (Figures S18 and S19, Supporting Information). Long-term stability was evaluated from the LSVs after long-term CV cycling and chronoamperometry measurement. It was noteworthy that

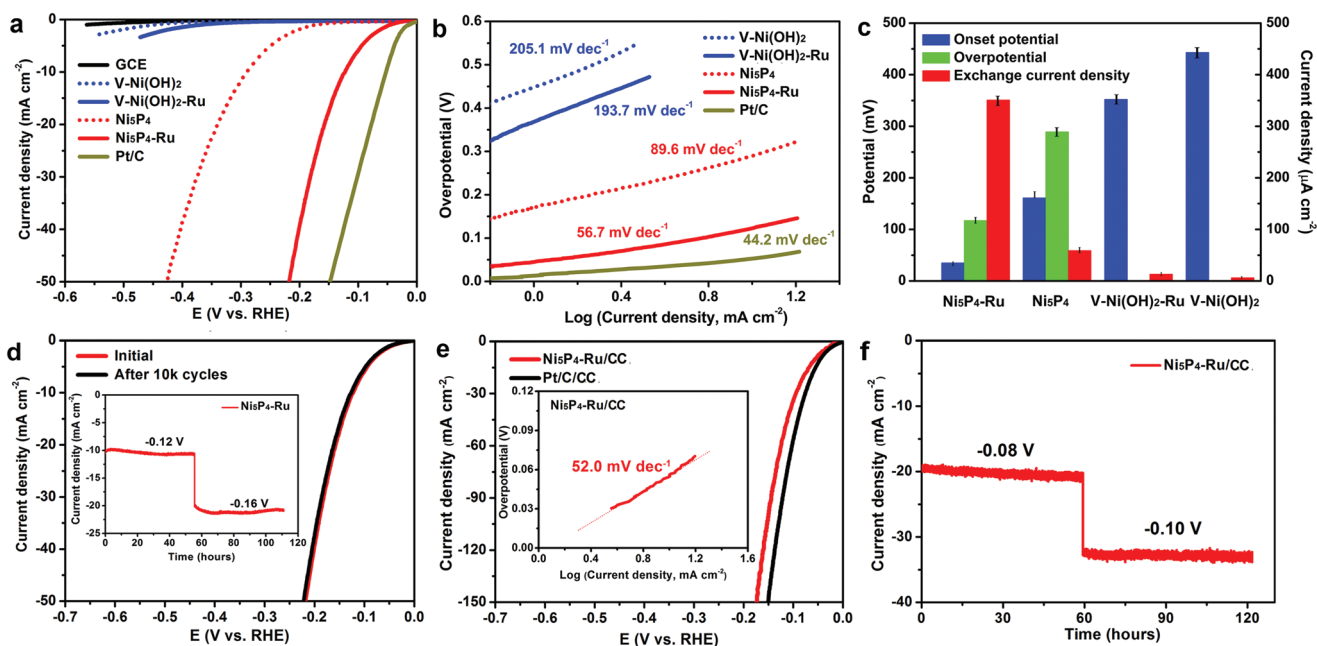


Figure 2. a) LSV curves of the obtained samples measured in 1.0 M KOH solution. b) The corresponding Tafel slopes of these samples. c) The calculated electrochemical parameters of these samples, error bar was from three individual measurements. d) The LSVs after long-term CV cycling and chronoamperometry measurement at given potentials measured for over 5 days. e) The LSV curves of samples loaded on carbon cloth collector, and the calculated Tafel slope. f) Long-term stability measurement of Ni₅P₄-Ru loaded on carbon cloth.

the overpotential and current density showed negligible changes under catalytic condition, suggesting its superior catalytic stability (Figure 2d). The atomic Ru sites after stability test could still be maintained and be illustrated by the post-testing XAFS spectrum, in which the peak information about Ru center was almost unchanged (Figure S20, Supporting Information). To be applied in practice, the performance of catalysts loaded onto large collectors would also be important. Next, the Ni₅P₄-Ru catalyst was loaded onto carbon cloth (noted as Ni₅P₄-Ru/CC) to measure the HER activity. In Figure 2e, the Ni₅P₄-Ru/CC shows an overpotential of only 54 mV at a current density of 10 mA cm⁻², low onset potential of 17 mV and small Tafel slope of 52.0 mV decade⁻¹, which surpass most of the reported catalysts and is comparable to Pt/C (Table S5, Supporting Information). The electrochemical stability was also maintained even after a consecutive test over 5 days (Figure 2f).

From the electrochemical results, it was concluded that the boosted HER performance should stem from the single-atomic Ru incorporation and subsequent structure optimization. The improved intrinsic performance really depends on the optimized structures.^[20] Therefore, the detailed structures of the phosphides with/without single-atomic Ru incorporation should be explored. XPS was carried out to probe the surface changes of different samples. It could be observed that the Ni 2p binding energy in Ni₅P₄-Ru exhibited the positive shift of 0.25 eV than that in Ni₅P₄ (Figure 3a; Figure S21, Supporting Information). To some extent, this result implied the local electron density perturbation after Ru incorporation and the Ni sites probably served as electron donor.^[31] This conclusion could also be demonstrated from the Ni L-edge XANES profiles. The increased peak intensities of Ni L₃ and L₂ peaks of

Ni₅P₄-Ru stated its relatively decreased electron density due to electron donation to Ru sites (Figure 3b).^[31]

XAFS was also employed to explore their structural information. In Figure 3c, the XANES profiles of both Ni₅P₄-Ru and Ni₅P₄ at Ni K-edge are similar, but obviously different with that of Ni foil and NiO counterparts. The similar absorption spectra demonstrated that the host Ni₅P₄ structure was still preserved, which was consistent with the above XRD results. However, there was a positive absorption edge shift of Ni₅P₄-Ru (inset), indicating the occurrence of electron transfer from Ni sites to Ru.^[27] This electron transfer consequence was further confirmed by the linear combination fit of XANES spectra, which showed an increased average valence state of Ni in Ni₅P₄-Ru relative to Ni in Ni₅P₄ (Figure S22, Supporting Information). The oscillation curves and EXAFS profiles further proved the preservation of host structure (Figure S23; Figure 3d, Supporting Information). It was worth noting that the peak position of Ni–Ni bond in Ni₅P₄-Ru was slightly larger than that in Ni₅P₄ and this difference should be from the formation of larger Ni–Ru bond than Ni–Ni (Figure S14 and Table S3, Supporting Information). The localized structure perturbation after Ru incorporation was considered as the origin of the boosted electrocatalytic activity.

To understand the effect of single-atomic Ru incorporation into Ni₅P₄ on its structural and catalytic properties, DFT calculations were performed. First, the structures of Ni₅P₄ without/with Ru incorporation were established and showed several possible catalytic sites (Figure S24, Supporting Information).^[32] Structural parameters of the established model structure were well consistent with the experimental analysis (Figures S14, S15, and S25 and Tables S3 and S4, Supporting Information). The calculated density of states (DOS) demonstrated that the

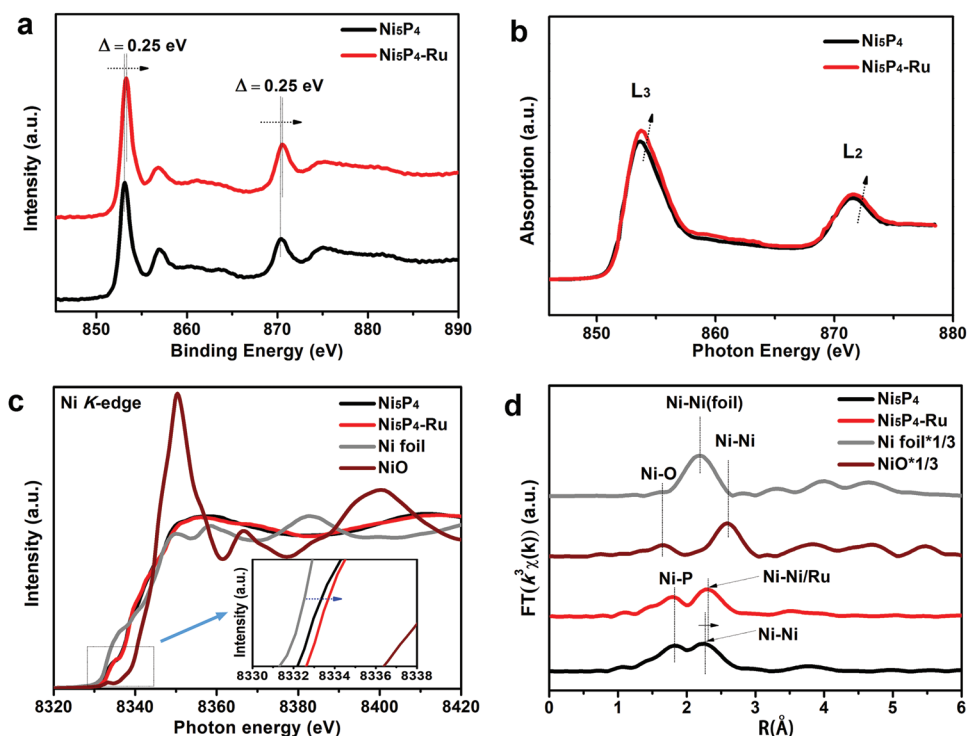


Figure 3. a) Ni 2p XPS comparison between $\text{Ni}_5\text{P}_4\text{-Ru}$ and Ni_5P_4 . b) Ni L-edge XANES comparison between $\text{Ni}_5\text{P}_4\text{-Ru}$ and Ni_5P_4 . c,d) XANES and EXAFS results of $\text{Ni}_5\text{P}_4\text{-Ru}$, Ni_5P_4 , Ni foil, and NiO at Ni K-edge, respectively.

$\text{Ni}_5\text{P}_4\text{-Ru}$ possesses higher DOS near the Fermi level than the pristine Ni_5P_4 (Figure 4a). This suggested that the conductivity of $\text{Ni}_5\text{P}_4\text{-Ru}$ has been improved, as experimentally confirmed by the measured small charge transfer resistance from EIS

(Figure S17, Supporting Information), thereby facilitating the catalytic HER process. From the electron density difference (EDD) analysis (Figure 4b), it further demonstrated the charge density redistributions and an obvious electron accumulation

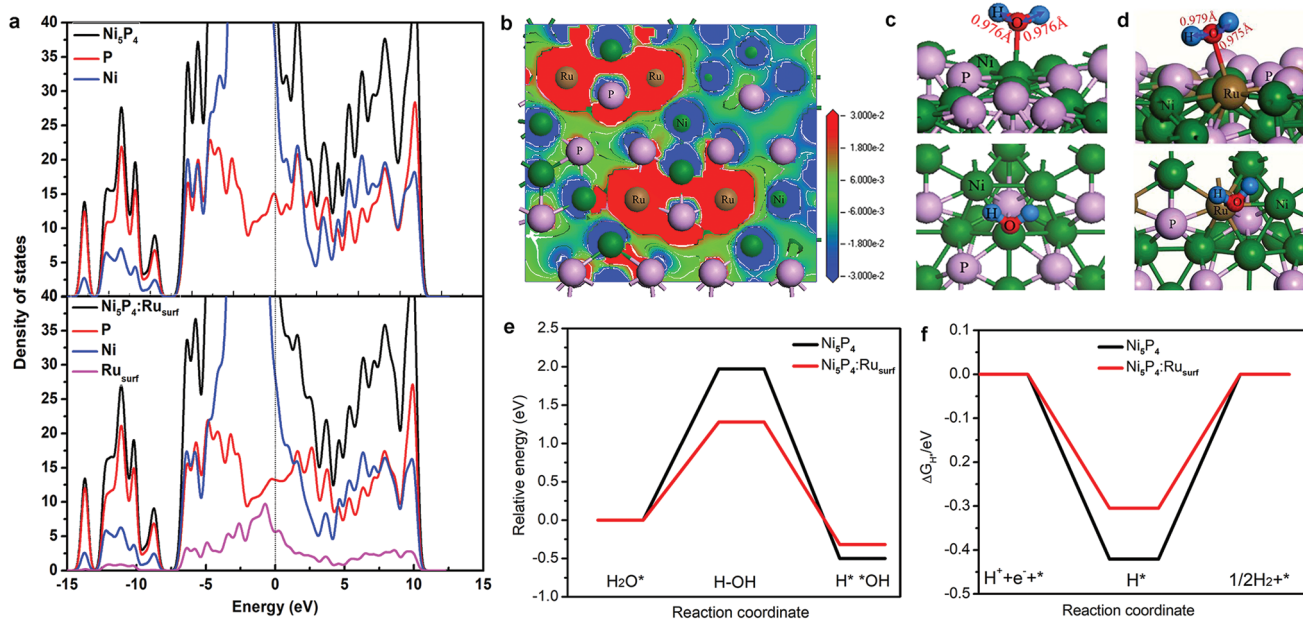


Figure 4. a) Calculated DOS for bare Ni_5P_4 and Ru-doped Ni_5P_4 . b) Bader analysis of Ni_5P_4 with Ru doping. c,d) The optimized structure for water adsorption on different sites. Brown, green and purple represent Ru, Ni, and P atoms. e) The energy barriers ($\Delta G(\text{H}_2\text{O})$) for water dissociation on optimized sites. f) The calculated adsorption free energy of hydrogen on different sites.

on Ru site was achieved. The localized structural polarization produced an environment with electron-rich Ru sites, which brought the reduced energy barrier of water dissociation. In addition, we also calculated the binding energy of H₂O on pristine Ni₅P₄ and Ni₅P₄-Ru (Tables S6 and S7, Supporting Information). The calculated results showed that the H₂O molecular was thermodynamically more favorable adsorption on Ni₅P₄-Ru (the former binding energy was -0.36 eV at Ni-top site, the latter was -0.41 eV at Ru-top site). The structures for H₂O dissociation were also established (Figures S26 and S27, Supporting Information; Figure 4c,d). The calculated lower energy barrier of the water dissociation step on the Ru site in Ni₅P₄-Ru (1.28 eV) than that on bare Ni₅P₄ (1.97 eV) proved that the incorporated Ru sites were more efficient than Ni site to dissociate H₂O (Figure 4e). Additionally, the optimized hydrogen adsorption free energy (ΔG_{H^*}) was meantime achieved (Figure 4f). For the mode of Ni₅P₄-Ru, it processed a G_{H^*} value of -0.30 eV (at the site of hollow 2), which was lower than that of pristine Ni₅P₄ (its value was -0.42 eV at the site of P). This suggested that the Ru-doped site possessed favorable energetics to reduce absorbed H* (Figures S24 and S28 and Tables S8 and S9, Supporting Information; Figure 4f). It was interesting that the dissociated H₂O was expected to move to sites nearby Ru, therefore the active Ru site would be released to dissociate next H₂O (Tables S10 and S11, Supporting Information). In brief, the incorporated Ru site expectedly brings the good water dissociation energetics. Next, the localized structural polarization further achieves favorable H adsorption process to boost the HER catalysis.

In summary, the nickel-vacancy-mediated synthesis strategy has achieved the synthesis of the Ni₅P₄ nanoparticles incorporating single-atomic Ru with high loading. The meticulous spectroscopic analysis, combined with DFT calculations, reveal that the localized structural polarization brings the introduced single-atomic Ru sites with increased electron density, thereby optimizing the H₂O dissociation process. The single-atom Ru sites also provide positive roles in optimizing reaction intermediates energetics to boost overall HER activity. This study demonstrates that the proper integration design of structural regulation and active site incorporation will provide high potential to obtain efficient electrocatalysts.

Experimental Section

Synthesis of V-Ni(OH)₂, P-Ni(OH)₂, V-Ni(OH)₂-Ru, and P-Ni(OH)₂-Ru: All chemicals were of analytical grade and used as received. The V-Ni(OH)₂ was prepared using propylene oxide (PO)-mediated alkanization precipitation method.^[26]

Typically, 3 mmol NiCl₂·6H₂O (713 mg) was dissolved in 9 mL ethanol under magnetic stirring to form a homogeneous solution. After stirring for 20 min, 2.6 mL PO was drop-casted into the above solution, then the obtained solution was stirred for another 24 h. The obtained precipitation was washed with ethanol several times to get rid of organics, ions, and other possible residues and finally dried at 60 °C overnight under vacuum. For P-Ni(OH)₂, the synthesis process is almost the same with V-Ni(OH)₂, except for the usage of ethanol changed to be water. For the V-Ni(OH)₂-Ru (or P-Ni(OH)₂-Ru), 100 mg of the obtained V-Ni(OH)₂ (or P-Ni(OH)₂) was dispersed into 50 mL water under stirring, and then 10 mL 0.005 M RuCl₃ aqueous solution was dropped into the above dispersion and kept stirring for another

24 h. The obtained samples were collected after washing with water for several times and vacuum drying. To obtain the Ni₅P₄ and Ni₅P₄-Ru samples, the V-Ni(OH)₂ (or V-Ni(OH)₂-Ru) was treated with sodium hypophosphite (NaH₂PO₂) under Ar flow condition (100 sccm). In brief, 20 mg sample was tiled at the combustion boat near Ar-outlet side, and 200 mg NaH₂PO₂ was put onto the near Ar-inlet side; later, these samples were heated at 400 °C for 2 h with a rising rate of 10 °C h⁻¹. Attention, the sweep gas should be absorbed with saturated CuSO₄ solution. After cooling down to room temperature, the final product was collected by washing with ethanol several times.

Materials Characterization: The samples' structures were first examined by XRD on a Philips X'Pert Pro Super diffractometer equipped with Cu K α radiation ($\lambda = 1.54178 \text{ \AA}$). The chemical states of different samples were analyzed by XPS measurements on a Thermo ESCALAB 250 spectrometer with monochrome Al anode (Al K $\alpha = 1486.6 \text{ eV}$) and EPR on a JES-FA200 at 140 K in an Ar atmosphere. The used microfrequency is from 9082 to 9086 MHz and the used micro power is 0.998000 mW. C 1s binding energy (284.8 eV) was used as calibration of XPS binding energies. Typical morphology and structure observations of the as-prepared samples were obtained from TEM and HRTEM on JEM-2100F field-emission electron microscopy with an acceleration voltage of 200 kV. The corresponding energy-dispersive X-ray spectroscopy (EDS) mapping was also performed. The atomic and electronic structures were evaluated from Ni/Ru K-edge XAFS measurements from Shanghai Synchrotron Radiation Facility (BL14W1, SSRF), Ni L-edge X-ray absorption near edge structures (XANES) measurement from BL12B- α of Hefei National Synchrotron Radiation Laboratory (NSRL), and STEM on a JEOL JEM-ARF200F (200 kV) with a spherical aberration corrector. The elemental ratios were evaluated with ICP-AES using an Optima 7300DV.

Electrochemical Measurements: The electrochemical measurements were carried out on CHI 760E electrochemical workstation (CH Instruments, China) with a standard three-electrode cell consisting of counter electrode (carbon rod, CR), working electrode (samples deposited on usual glassy carbon electrodes with a diameter of 3 mm or carbon cloth), and reference electrode (Ag/AgCl saturated with 3.5 M KCl). The electrolyte was 1.0 M KOH solution with Ar purging for HER measurement. Typically, for electrode preparation, 4 mg of the sample was dispersed in the mixed solution of 0.75 mL ethanol, 0.25 mL water, and 0.05 mL 5 wt% nafion solution by sonication for over 30 minutes. A measure of 5 μL of the above suspension was drop-casted to usual glassy carbon electrode (area = 0.07065 cm²; loading mass density = 0.142 mg cm⁻²) or 40 μL suspension was loaded on carbon cloth (valid area = 1 cm², loading density = 0.152 mg cm⁻²), and dried at room temperature. In this work, the final potential was calibrated into reversible hydrogen electrode (RHE), unless otherwise noted. First, cyclic voltammetry (CV) measurements were performed for over 100 cycles (scan rate: 100 mV s⁻¹) to reach a stable state. After CVs, LSV curves were recorded with scan rate of 5 mV s⁻¹ for HER. By plotting potential η against $\log |j|$ from LSV curves, Tafel slopes can be gained. The exchanged current density was calculated from the cross points between Tafel curves and x-axis (at theoretically equilibrium potential of 0 V). To evaluate the electrochemical durability, chronoamperometry measurement at applied potentials and CV cycling were collected. The electrochemical surface areas (ECSA) were evaluated by CV curves at the potential window of -0.90 to -0.70 V versus Ag/AgCl with different scan rates of 20, 40, 60, 80, 100, and 120 mV s⁻¹, respectively. By plotting the $\Delta j/2_{-0.80 \text{ V versus Ag/AgCl}}$ -scan rate curves, the linear slopes were used to represent the ECSA values. The Nyquist plots were measured at frequencies ranging from 100 kHz to 0.01 Hz at the open potential with an amplitude voltage of 5 mV.

DFT Calculations: All the calculations were performed using the DMOL³ program, based on the spin-polarized density functional theory (DFT) method.^[33] The Perdew-Burke-Ernzerhof (PBE) functional of generalized gradient approximation (GGA) was selected as the electron exchange-correlation potential.^[34] The nickel 3d and 4s electrons, phosphorus 3s and 3p electrons, ruthenium 4d and 5s, hydrogen 1s electron and oxygen 2s and 2p electrons are treated as valence electrons.

Effective core potentials (ECP) were used to treat the core electrons. The spin-unrestricted approach is used to calculate the adsorption properties. Molecule orbitals were expanded into a double-numerical basis with polarization function (DNP) basis set (version 3.5). The convergence tolerance of the energy charge, maximum force, and the displacement are set to 1×10^{-5} Hartree (Ha), $0.002 \text{ Ha } \text{Å}^{-1}$, and 0.005 Å . Brillouin one integration is performed using $3 \times 3 \times 3$ and $3 \times 3 \times 1$ Monkhorst–Pack mesh k -point for geometry optimization and calculate the properties of bulk and surface, respectively. The calculated lattice constants of Ni_5P_4 bulk are $a = b = 6.83020 \text{ Å}$ and $c = 11.0623 \text{ Å}$, these values are in good agreement with the experimental values.^[35] The Ni_5P_4 (001) surface is modeled by using a four layer with $2x\sqrt{3}$ surface slab. For Ru-doped Ni_5P_4 (001) surface, it was constructed by replacing Ni atom with Ru atom on Ni_5P_4 (001) surface. A vacuum layer of $\approx 15 \text{ Å}$ thick was added in the slab to guarantee that there are no unphysical interactions between the slab and the periodic images perpendicular to the surface affecting the calculations. Meanwhile, atoms in the bottom two layers were fixed and all other atoms including adsorbates can be relaxed.

The binding energy (BE) was calculated as

$$E_{\text{binding energy}} = E_{(\text{slab-adsorbate})} - E_{(\text{slab})} - E_{(\text{adsorbate})} \quad (1)$$

where $E_{(\text{slab-adsorbate})}$, $E_{(\text{slab})}$, and $E_{(\text{adsorbate})}$ are the total energy of slab with adsorbate, the total energy of clean slab, and the energy of adsorbate in the gas phase, respectively. The adsorption energies of H^* intermediates on Ni_5P_4 (001) surface is -0.63 eV (see Table S6 in the Supporting Information), which is in good agreement with former calculation results (-0.64 eV).^[32]

The Gibbs free energy (G) of a species is calculated as^[36]

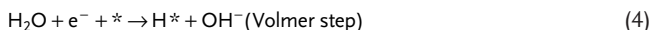
$$G = E + \text{ZPE} - TS \quad (2)$$

Here, E is the total energy of a species obtained from DFT calculations, ZPE and S are the zero-point energy and entropy of a species respectively, and $T = 298.15 \text{ K}$. The change in free energy (ΔG) is calculated as^[36]

$$\Delta G = \Delta E + \Delta \text{ZPE} - T\Delta S \quad (3)$$

where ΔE is the binding energy of adsorbed species.

The free energy of HER in alkaline has been calculated by considering the following sequential steps^[34,37]



or



where $*$ denotes surface species/sites.

The transition state of a chemical reaction was located by using complete LST/QST approach.^[36] The activation energy (E_a) of a chemical reaction is defined as the energy difference between the transition and initial states, while the reaction energy (ΔE) is defined as the energy difference between the final and initial states.

Supporting Information

Supporting Information is available from the Wiley Online Library or from the author.

Acknowledgements

Q.H., D.T., and H.J. contributed equally to this work. This work was financially supported by National Key R&D Program of China (2017YFA0303500), NSFC (U1932201, 11574280, 21727801, and 21978278), Innovative Research Groups of NSFC (11621063), NSFC-MAECI (51861135202), CAS Key Research Program of Frontier Sciences (QYZDB-SSW-SLH018), and CAS Interdisciplinary Innovation Team.

L.S. acknowledges the support from Key Laboratory of Advanced Energy Materials Chemistry (Ministry of Education), Nankai University (111 Project, B12015). The authors thank the Shanghai Synchrotron Radiation Facility (14W1, SSRF) and the Hefei Synchrotron Radiation Facility (Photoemission and Catalysis/Surface Science Endstations at NSRL) for helps in characterizations.

Conflict of Interest

The authors declare no conflict of interest.

Keywords

alkaline hydrogen evolution, density functional theory, single atoms, structure polarization, X-ray absorption spectroscopy

Received: October 24, 2019

Revised: December 26, 2019

Published online:

- [1] H. I. Karunadasa, C. J. Chang, J. R. Long, *Nature* **2010**, *464*, 1329.
- [2] D. Voiry, H. Yamaguchi, J. Li, R. Silva, D. C. B. Alves, T. Fujita, M. Chen, T. Asefa, V. B. Shenoy, G. Eda, M. Chhowalla, *Nat. Mater.* **2013**, *12*, 850.
- [3] R. Ye, P. Angel-Vicente, Y. Liu, M. J. Arellano-Jimenez, Z. Peng, T. Wang, Y. Li, B. I. Yakobson, S.-H. Wei, M. J. Yacaman, J. M. Tour, *Adv. Mater.* **2016**, *28*, 1427.
- [4] R. Ma, Y. Zhou, Y. Chen, P. Li, Q. Liu, J. Wang, *Angew. Chem., Int. Ed.* **2015**, *54*, 14723.
- [5] J. Zhang, J. Wu, X. Zou, K. Hackenberg, W. Zhou, W. Chen, J. Yuan, K. Keyshar, G. Gupta, A. Mohite, P. M. Ajayan, J. Lou, *Mater. Today* **2019**, *25*, 28.
- [6] M. Chhetri, S. Sultan, C. N. R. Rao, *Proc. Natl. Acad. Sci. USA* **2017**, *114*, 18986.
- [7] Y. Zhu, H. A. Tahini, Z. Hu, J. Dai, Y. Chen, H. Sun, W. Zhou, M. Liu, S. C. Smith, H. Wang, Z. Shao, *Nat. Commun.* **2019**, *10*, 149.
- [8] Y. Zang, S. Niu, Y. Wu, X. Zheng, J. Cai, J. Ye, Y. Xie, Y. Liu, J. Zhou, J. Zhu, X. Liu, G. Wang, Y. Qian, *Nat. Commun.* **2019**, *10*, 1217.
- [9] B. You, Y. Zhang, Y. Jiao, K. Davey, S. Z. Qiao, *Angew. Chem., Int. Ed.* **2019**, *58*, 11796.
- [10] C. Hu, L. Zhang, J. Gong, *Energy Environ. Sci.* **2019**, *12*, 2620.
- [11] K. Xu, Y. Sun, Y. Sun, Y. Zhang, G. Jia, Q. Zhang, L. Gu, S. Li, Y. Li, H. J. Fan, *ACS Energy Lett.* **2018**, *3*, 2750.
- [12] Y.-R. Zheng, P. Wu, M.-R. Gao, X.-L. Zhang, F.-Y. Gao, H.-X. Ju, R. Wu, Q. Gao, R. You, W.-X. Huang, S.-J. Liu, S.-W. Hu, J. Zhu, Z. Li, S.-H. Yu, *Nat. Commun.* **2018**, *9*, 2533.
- [13] Q. Xu, Y. Liu, H. Jiang, Y. Hu, H. Liu, C. Li, *Adv. Energy Mater.* **2019**, *9*, 1802553.
- [14] P. Chen, T. Zhou, M. Chen, Y. Tong, N. Zhang, X. Peng, W. Chu, X. Wu, C. Wu, Y. Xie, *ACS Catal.* **2017**, *7*, 7405.
- [15] J. Zhang, Y. Liu, C. Sun, P. Xi, S. Peng, D. Gao, D. Xue, *ACS Energy Lett.* **2018**, *3*, 779.
- [16] Q. Qin, H. Jang, L. Chen, G. Nam, X. Liu, J. Cho, *Adv. Energy Mater.* **2018**, *8*, 1801478.
- [17] J. Yang, B. Chen, X. Liu, W. Liu, Z. Li, J. Dong, W. Chen, W. Yan, T. Yao, X. Duan, Y. Wu, Y. Li, *Angew. Chem., Int. Ed.* **2018**, *57*, 9495.
- [18] J. Zhang, Y. Zhao, X. Guo, C. Chen, C.-L. Dong, R.-S. Liu, C.-P. Han, Y. Li, Y. Gogotsi, G. Wang, *Nat. Catal.* **2018**, *1*, 985.
- [19] X.-F. Yang, A. Wang, B. Qiao, J. Li, J. Liu, T. Zhang, *Acc. Chem. Res.* **2013**, *46*, 1740.

- [20] Y. Wang, J. Mao, X. Meng, L. Yu, D. Deng, X. Bao, *Chem. Rev.* **2019**, *119*, 1806.
- [21] G. Chen, Y. Zhao, G. Fu, P. N. Duchesne, L. Gu, Y. Zheng, X. Weng, M. Chen, P. Zhang, C.-W. Pao, J.-F. Lee, N. Zheng, *Science* **2014**, *344*, 495.
- [22] B. Qiao, A. Wang, X. Yang, L. F. Allard, Z. Jiang, Y. Cui, J. Liu, J. Li, T. Zhang, *Nat. Chem.* **2011**, *3*, 634.
- [23] J.-C. Liu, Y.-G. Wang, J. Li, *J. Am. Chem. Soc.* **2017**, *139*, 6190.
- [24] L. Lin, W. Zhou, R. Gao, S. Yao, X. Zhang, W. Xu, S. Zheng, Z. Jiang, Q. Yu, Y.-W. Li, C. Shi, X.-D. Wen, D. Ma, *Nature* **2017**, *544*, 80.
- [25] B. Lu, L. Guo, F. Wu, Y. Peng, J. E. Lu, T. J. Smart, N. Wang, Y. Z. Finckel, D. Morris, P. Zhang, N. Li, P. Gao, Y. Ping, S. Chen, *Nat. Commun.* **2019**, *10*, 631.
- [26] Q. He, Y. Wan, H. Jiang, Z. Pan, C. Wu, M. Wang, X. Wu, B. Ye, P. M. Ajayan, L. Song, *ACS Energy Lett.* **2018**, *3*, 1373.
- [27] D. A. Grishina, A. A. Mironov, I. S. Pentegov, A. V. Marikutsa, E. A. Konstantinova, *Proc. SPIE* **2012**, *8430*, 84300A.
- [28] J. Zhang, X. Wu, W.-C. Cheong, W. Chen, R. Lin, J. Li, L. Zheng, W. Yan, L. Gu, C. Chen, Q. Peng, D. Wang, Y. Li, *Nat. Commun.* **2018**, *9*, 1002.
- [29] Z. Wang, S.-M. Xu, Y. Xu, L. Tan, X. Wang, Y. Zhao, H. Duan, Y.-F. Song, *Chem. Sci.* **2019**, *10*, 378.
- [30] X. Sun, C. Chen, S. Liu, S. Hong, Q. Zhu, Q. Qian, B. Han, J. Zhang, L. Zheng, *Angew. Chem., Int. Ed.* **2019**, *58*, 4669.
- [31] H. Jiang, Y. Lin, B. Chen, Y. Zhang, H. Liu, X. Duan, D. Chen, L. Song, *Mater. Today* **2018**, *21*, 602.
- [32] T. Zhang, K. Yang, C. Wang, S. Li, Q. Zhang, X. Chang, J. Li, S. Li, S. Jia, J. Wang, L. Fu, *Adv. Energy Mater.* **2018**, *8*, 1801690.
- [33] D. Tian, K. Li, Y. Wei, X. Zhu, C. Zeng, X. Cheng, Y. Zheng, H. Wang, *Phys. Chem. Chem. Phys.* **2018**, *20*, 11912.
- [34] Y. Wu, X. Liu, D. Han, X. Song, L. Shi, Y. Song, S. Niu, Y. Xie, J. Cai, S. Wu, J. Kang, J. Zhou, Z. Chen, X. Zheng, X. Xiao, G. Wang, *Nat. Commun.* **2018**, *9*, 1425.
- [35] A. B. Laursen, K. R. Patraju, M. J. Whitaker, M. Retuerto, T. Sarkar, N. Yao, K. V. Ramanujachary, M. Greenblatt, G. C. Dismukes, *Energy Environ. Sci.* **2015**, *8*, 1027.
- [36] J. K. Nørskov, J. Rossmeisl, A. Logadottir, L. Lindqvist, J. R. Kitchin, T. Bligaard, H. Jónsson, *J. Phys. Chem. B* **2004**, *108*, 17886.
- [37] W. C. Sheng, M. Myint, J. G. Chen, Y. S. Yan, *Energy Environ. Sci.* **2013**, *6*, 1509.